Improved VIIRS Day/Night Band Imagery With Near-Constant Contrast

Calvin K. Liang, Stephen Mills, Bruce I. Hauss, and Steven D. Miller

***Abstract*—The Suomi-NPP Visible Infrared Imager Radiometer Suite (VIIRS) instrument provides the next generation of visible/infrared imaging including the day/night band (DNB) with nominal bandwidth from 500 to 900 nm. Previous to VIIRS, the Defense Meteorological Satellite Program Operational Linescan System (OLS) measured radiances that spanned over seven orders of magnitude, using an onboard gain adjustment to provide the capability to image atmospheric features across the solar terminator, to observe nighttime light emissions over the globe, and to monitor the global distribution of clouds. The VIIRS DNB detects radiances that span over eight orders of magnitude, and because it has 13–14-b quantization (compared with 6 b for OLS) with three gain stages, the DNB has its full dynamic range at every part of the scan. One process that is applied to the VIIRS DNB radiances is a solar/lunar zenith angle dependent gain adjustment to create near-constant contrast (NCC) imagery. The at-launch NCC algorithm was designed to reproduce the OLS capability and, thus, was constrained to solar and lunar angles from 0° to 105°. This limitation has, in part, lead to suboptimal imagery due to the assumption that DNB radiances fall off exponentially beyond twilight. The VIIRS DNB ultrasensitivity in low-light conditions enables it to detect faint emissions from a phenomenon called airglow, thus invalidating the exponential fall-off assumption. Another complication to the NCC imagery algorithm is the stray light contamination that contaminates the DNB radiances in the astronomical twilight region. We address these issues and develop a solution that leads to high-quality imagery for *all* solar and lunar conditions.**

***Index Terms*—Day/night band (DNB), near-constant contrast (NCC), Suomi National Polar-orbiting Partnership (S-NPP), terminator visible imaging, Visible Infrared Imager Radiometer Suite (VIIRS).**

I. Introduction

HISTORICALLY, visible/near infrared (Vis/NIR) band nighttime imagery was only provided operationally from space by the Operational Linescan System (OLS) onboard the Department of Defense's Defense Meteorological Satellite Program spacecraft. The OLS terminator imagery is capable of sensing radiances that span over seven orders of magnitude, providing the ability to detect atmospheric conditions spanning from daytime, across the terminator, through partial moon illumination conditions [1]. OLS imagery spatial resolution is nominally ∼2.8 km. To view imagery that spans this dynamic range of radiances is impossible even if radiances were displayed on a base-10 logarithmic scale. In order to make the terminator imagery viewable, the OLS Gain Management Algorithm (GMA), implemented onboard the OLS analog signal processor, applies a Gain Value Versus Scene Solar Elevation (GVVSSE) table that adjusts the detected radiance dynamically to provide imagery that is nearly constant in apparent contrast, i.e., the relative contrast in the scene when viewed under day, terminator, and night illumination conditions is almost indistinguishable. Here, conditions defining day through the terminator correspond to solar angles spanning 0°–105°. Fig. 1 shows an example of the GVVSSE table [4]. A companion lunar (GVVSLE) table accounts for lunar source signals. Modeled bidirectional scattering distribution function (BSDF) effects are also accounted for in both the GVVSSE and GVVSLE tables. The modeled BSDF is a function of solar zenith, sensor zenith, and relative azimuth angle.[1] This adjustment must be done onboard because the instrument has only 6-b quantization without multiple gain stages. Thus, the sensor must sequentially navigate through each stage and then apply the GVVSSE/GVVSLE adjustment via the onboard GMA. Therefore, at any given time in the scan, the OLS has less than two orders of magnitude of dynamic range. Another consequence of the 6-b quantization of the high-gain setting and the limited dynamic range of OLS is that city lights in urban centers become saturated [15], although recent studies by [2] and [14] have shown promising methods to correct the high-gain saturation problem.

The recently launched (October 28, 2011) Suomi National Polar-orbiting Partnership (S-NPP) satellite, carrying the Visible Infrared Imager Radiometer Suite (VIIRS) instrument, is able to detect radiances that span a dynamic range of over eight orders of magnitude through its day/night band (DNB) that nominally spans 500–900 nm. The VIIRS DNB has a signal-to-noise ratio (SNR) of ∼9 or greater at the required minimum radiance level of $L_{\min} = 3 \times 10^{-9}$ W/cm^2/sr [3]. With superior radiometric resolution compared to the OLS, VIIRS is able to simultaneously digitize four gain stages: low-gain stage (LGS, 13 b), mid-gain stage (MGS, 13 b), and two redundant high-gain stages (HGS, 14 b); the redundancy in HGS (HGA and HGB) serves to filter out signals corresponding

Manuscript received December 4, 2013; revised January 6, 2014; accepted February 6, 2014. Date of publication March 11, 2014; date of current version May 30, 2014. The work of S. D. Miller was supported by the NOAA Joint Polar-orbiting Satellite System Cal/Val and Algorithm Program, the Naval Research Laboratory (BAA Contract N00173-10-C2003), and the Oceanographer of the Navy through PEO C4I/PMW-120 under program element PE-0603207N.

C. K. Liang is with Northrop Grumman Corporation, Redondo Beach, CA 90278 USA (e-mail: Calvin.Liang@ngc.com).

S. Mills is with Renaissance Man Engineering, Glendale, CA 91202 USA.

B. I. Hauss is with DKK Company Inc., Ruston, LA 71270 USA.

S. D. Miller is with the Cooperative Institute for Research in the Atmosphere, Colorado State University, Fort Collins, CO 80523-1375 USA.

Digital Object Identifier 10.1109/TGRS.2014.2306132

[1]The BSDF does not partition reflectance and scattering by surface type but rather represents the mean reflectance or scattering of the Earth surface and atmosphere (e.g., clouds).

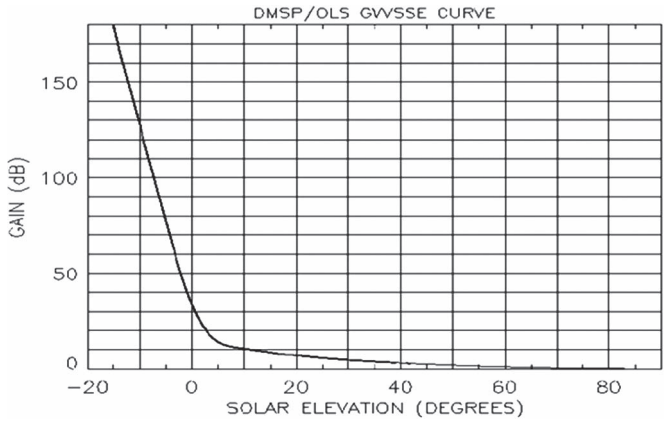

Fig. 1. Typical GVVSSE curve for OLS onboard variable gain control. Curve is designed so that a source with an albedo $= 0.8$ produces a 5-V output signal from the L-channel (0.4–1.1 μm) analog signal processor.

to high-energy particles striking the VIIRS focal plan array. These stages are digitized simultaneously onboard, and then, the appropriate gain stage is selected for each pixel, and the data are downlinked with the appropriate gain flag. The full dynamic range of the radiances is maintained for every part of the scene, and there is the flexibility to apply the algorithmic adjustments on the ground. This provides the capability to make algorithm and/or LUT changes via ground software changes, unlike the OLS which was constrained to onboard adjustments [5]. The GMA heritage is preserved for the VIIRS near-constant contrast (NCC) algorithm; however, some modifications are necessary to account for new capabilities as well as shortcomings of the instrument.

Unanticipated capabilities and limitations of the DNB sensor have driven the need for modification of the NCC algorithm. Due to the VIIRS DNB extreme sensitivity to low-light conditions, it has the ability to capture atmospheric and surface features even on nights devoid of lunar illumination. The airglow (or nightglow) emissions provide the source illumination during these lunar conditions from a geometrically thin layer near 85–95 km [6]. Due to light leakage onto the DNB focal plane, there is also significant stray light contamination that contaminates the DNB radiances in the solar terminator [7]. Because of these situations, the NCC algorithm and, specifically, the input LUTs are modified to produce imagery for all solar, lunar, and nonlunar conditions.

This paper presents a methodology for improving the VIIRS/DNB NCC algorithm in light of on-orbit data assessments. Sections II and III detail the main NCC algorithm and the GVVSSE/GVVSLE LUT derivation, respectively. In Section IV, we describe the results of our analysis and list possible applications that may benefit from the NCC product.

II. VIIRS NCC Algorithm

The at-launch VIIRS NCC algorithm applies gain adjustments to the VIIRS DNB sensor data records (SDRs), i.e., radiances, via the GVVSSE and GVVSLE LUTs, which are functions of solar and lunar zenith angles, respectively. The VIIRS DNB radiances can be decomposed in the following manner:

$$L = L_s + L_l \tag{1}$$

where L_s and L_l are the solar and lunar components of the observed top-of-atmosphere (TOA) upwelling radiance (L). For each VIIRS pixel, the DNB radiances are gain-adjusted and converted to a "pseudo-albedo[2]" defined as

$$\alpha = \frac{L}{L_{\mathrm{ref},s} + L_{\mathrm{ref},l}} \tag{2}$$

and can be expressed as

$$L_{\mathrm{ref},s} = \mathrm{BSDF}_s(\theta_s, \theta_v, \Delta\phi_s) \cdot E_s \tag{3}$$
$$L_{\mathrm{ref},l} = \mathrm{BSDF}_l(\theta_l, \theta_v, \Delta\phi_l) \cdot E_l(\beta) \tag{4}$$

where

$$\mathrm{BSDF}_s(\theta_s, \theta_v, \Delta\phi_s) = \frac{f_s(\theta_s, \theta_v, \Delta\phi_s)}{G_s(\theta_s)} \tag{5}$$
$$\mathrm{BSDF}_l(\theta_l, \theta_v, \Delta\phi_l) = \frac{f_l(\theta_l, \theta_v, \Delta\phi_l)}{G_l(\theta_l)}. \tag{6}$$

Here, G_s and G_l are the GVVSSE and GVVSLE LUT values described in Section III, f_s and f_l are the solar and lunar asymmetric reflectance factors, respectively, and θ_s, θ_l, θ_v, $\Delta\phi_s$, and $\Delta\phi_l$ are the solar zenith, lunar zenith, sensor zenith, solar relative azimuth, and lunar relative azimuth angles, respectively. The functions are not partitioned by land type nor differentiated between day and night; therefore, $f_s = f_l$. Although $L_{\mathrm{ref},s}$ and $L_{\mathrm{ref},l}$ are derived from empirical data (via G_s and G_l), the terms f_s and f_l, computed by the Moderate Resolution Atmospheric Transmission (MODTRAN) model version 4.0, for a nearly Lambertian Earth, account for the asymmetry of the average BSDF over the Earth [9]. The terms E_s and E_l (also computed via MODTRAN 4.0 [9]) denote the solar and lunar *radiances* that would be observed with solar and lunar angles at zenith, respectively, given a surface with albedo $= 1$ [8]. It is also important to note that, while E_s is assumed to be constant,[3] E_l is a function of lunar phase angle β.[4]

The bidirectional reflectance distribution function (BRDF) is only meaningful for $\theta_s < 90^\circ$. In these cases, the BRDF is related to the BSDF, as defined here, by the following equation:

$$\mathrm{BSDF}_s = \mathrm{BRDF}_s \cdot \cos\theta_s \tag{7}$$

where

$$\mathrm{BRDF}_s(\theta_s, \theta_v, \Delta\phi_s) = \frac{f_s(\theta_s, \theta_v, \Delta\phi_s)}{G_s(\theta_s) \cdot \cos\theta_s.} \tag{8}$$

The same relationship applies to the lunar BRDF.

[2]We use the term "pseudo" because the computed albedo is, strictly speaking, not an albedo for parts of the scene where atmospheric scattering is a dominant contributor to the observed TOA radiance.

[3]This assumption ignores seasonal Earth-to-Sun distance changes since it has a small effect on imagery as an imagery product. This assumption causes a fluctuation of E_s of about 3% peak-to-valley over a season.

[4]In reality this is also a function of Moon-to-Earth surface. This distance varies from 93% to 106% of its average value. This causes E_l to vary about 25% peak-to-valley in addition to modulation from phase.

The at-launch operational NCC algorithm computes $L_{\mathrm{ref},s}$ and $L_{\mathrm{ref},l}$ for θ_s and θ_l ranging between 0° and 105° (at intervals of 0.1°) based on the heritage OLS GMA. The conversion from L to α is then done through (2)–(4). This conversion must provide NCC imagery across the terminator which preserves the relative contrast of atmospheric (e.g., clouds) and ground (e.g., ice surface) features, similar to a standard albedo. This is primarily accomplished through the gain factors G_s and G_l (5) and (6). The other BSDF effects of the global mean cloud cover are accounted for by the asymmetric reflectance factors (f_s, f_l). The final "pseudo-albedo" is considered an environmental data record (EDR) and is mapped using the ground-track Mercator algorithm.

III. GVVSSE and GVVSLE LUT Derivation

A. At-Launch GVVSSE and GVVSLE LUTs

For the VIIRS DNB, the GVVSSE and GVVSLE LUTs were empirically derived from calibrated DNB radiances collected over three days surrounding a new moon (i.e., no lunar illumination present). The radiances were filtered to remove high population density areas, which indirectly eliminates pixels with anthropogenic light sources. Then, an offline process relates L to θ_s empirically, via a functional fit. At each θ_s, the 80th percentile point of the L distribution, denoted by L_{80}, was selected as the point to fit through since this point provided adequate statistics for the entire range of θ_s.

The function L_{fit} is broken piecewise into three empirical functions

$$L^1_{\mathrm{fit}}(\theta_s) = a_0 + a_1 cos(\theta_s) \tag{9}$$
$$L^2_{\mathrm{fit}}(\theta_s) = e^{b_0+b_1\theta_s+b_2+\theta_s^2+b_3\theta_s^3+b_4\theta_s^4} \tag{10}$$
$$L^3_{\mathrm{fit}}(\theta_s) = e^{c_0+c_1\theta_s} \tag{11}$$

where (9)–(11) are valid for $0 \le \theta_s \le \theta_1$, $\theta_1 \le \theta_s \le \theta_2$, and $\theta_2 \le \theta_s \le 105$, respectively. Note: all fits are done on the natural log of the empirical functions. Equations (9)–(11) have boundary conditions that satisfy the following conditions:

$$L^i_{\mathrm{fit}}(\theta_i) = L^{i+1}_{\mathrm{fit}}(\theta_i) \tag{12}$$
$$\frac{dL^i_{\mathrm{fit}}(\theta_i)}{d\theta_s} = \frac{dL^{i+1}_{\mathrm{fit}}(\theta_i)}{d\theta_s} \tag{13}$$

where $i = 1, 2$ and correspond to (9)–(11). A χ^2 minimization process is used simultaneously on all three fit functions (9)–(11) to determine the best fit to L_{80}. Once the best fit is computed, the gain values are then calculated as such

$$G_s(\theta_s) = \frac{L_{\mathrm{fit}}(\theta_s = 0)}{L_{\mathrm{fit}}(\theta_s)} \tag{14}$$

where L_{fit} is the empirical fit of (9)–(11) to L_{80}, which, again, is derived from L collected over a three-day period. The lunar gains G_l are derived by simply replicating the solar gains (G_s) and substituting θ_s with θ_l, respectively. The NCC algorithm appropriately adjusts the gains G_s and G_l by the radiance values E_s and E_l in (3) and (4). The functional fits in (9)–(11) were derived to reproduce a curve of the same shape as that of Fig. 1. This was done under the assumption that, as the Earth's surface goes into twilight, the observed TOA radiances will fall off exponentially [see (11)]. For OLS, this is the observed behavior in Fig. 1.

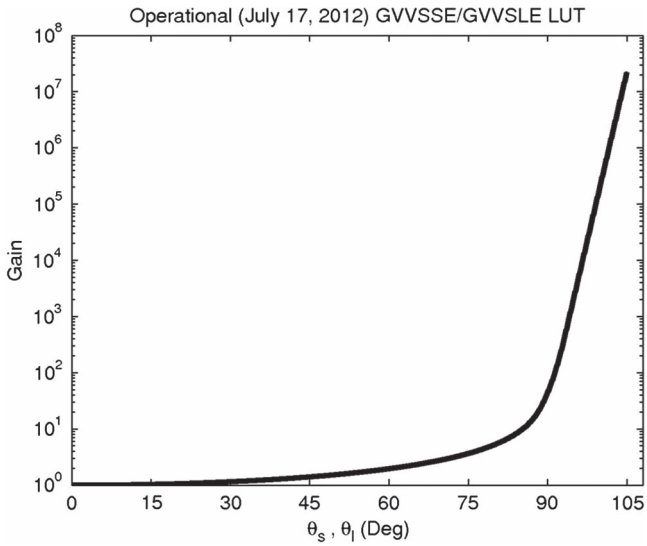

Fig. 2. GVVSSE/GVVSLE LUT made operational in the IDPS on July 17, 2012.

The operational GVVSSE/GVVSLE LUT (see Fig. 2)—as of July 17, 2012—was derived from DNB radiances measured between February 20 and 22, 2012 (new moon on the 21st). The curve shows an exponential increase in gain to account for the expected exponential decay in observed radiances as function of increasing θ_s, where the functional splice values for this table are $\theta_1 \approx 89°$ and $\theta_2 \approx 93°$. However, the VIIRS DNB is sensitive enough to observe radiances on the order of $\sim 10^{-10}$ W/cm^2/sr, providing an unanticipated sensitivity to atmospheric airglow emissions. The methodology employed for handling airglow will be described in Section III-C.

B. Stray Light Impacts on the GVVSSE/GVVSLE LUTs

As briefly described in Section I, stray light contamination produces elevated DNB radiances in the vicinity of the solar terminator. Around the time of the terminator crossing, this stray light is likely entering the VIIRS scan cavity directly and indirectly via reflectance off the solar diffuser attenuation screen (in the southern hemisphere) and nadir door opening (both hemispheres) [7]. Stray light impacts ~25% of nighttime scenes [7]. It manifests as a diffuse gray haze in the DNB SDRs, oriented in the scan line dimension, and its latitudinal extent shifts as a function of season (i.e., tracking the terminator position). It is crucial to remove the stray light before fitting L_{80} and deriving (14) (recall that L_{80} is derived from the operational DNB radiances L).

Fig. 3(a) and (b) shows joint distributions of L as a function of θ_s for all DNB radiances observed between August 16 and 18, 2012. Fig. 3(a) shows the distribution of L without the stray light removed. A clear discontinuity in the distribution can be seen between $\theta_s \sim 95°$ and 118°. This stray light formed discontinuity is not physical and, as mentioned, needs to be removed in order to properly fit L_{80}.

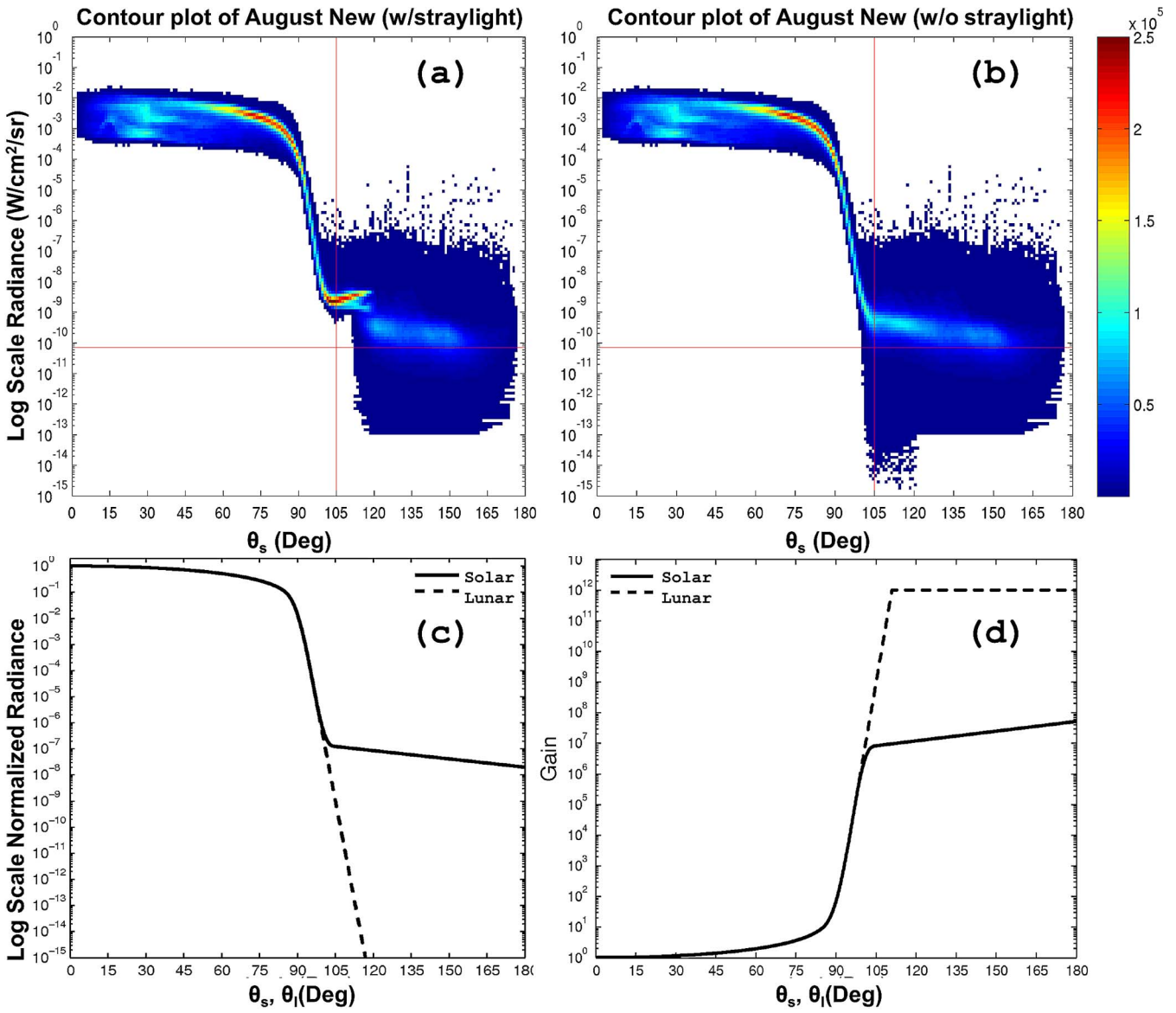

Fig. 3. Joint distribution of DNB radiance (L, plotted on log10 scale) versus s taken from new moon data between August 16 and 18, 2012, for L (a) without and (b) with stray light removed. Plotted in panel (c) are the final solar (solid) and lunar (dashed) fits to the radiance distribution in panel (b) normalized to θ_s and $\theta_l = 0$. Plotted in panel (d) are the gains, i.e., GVVSSE/GVVSLE LUTs, derived from the normalized radiances in panel (c). For panels (a) and (b), the vertical red line placed at $\theta_s = 105°$ and the red horizontal line placed at $7e{-}11$ W/cm^2/sr (VIIRS DNB noise floor) are displayed for reference. The retention of signal for $\theta_s > 105°$ is due to airglow detection (direct emission and cloud/surface reflected).

We use the methodology described in [7] to remove the stray light. Briefly, the stray light is estimated from new moon twilight and nighttime data (from August 16–18, 2012) by selecting the darkest granules, filtering out illumination sources such as city lights and auroras, and deriving LUTs of stray light radiances that are a function of sensor-local solar zenith angle (i.e., with respect to the spacecraft), detector, half-angle mirror (HAM) side, along scan frame, and Earth hemisphere. These LUTs are then used to correct all of the new moon DNB granules. Once these granules are corrected, the resulting SDRs are used for the L distribution statistics (9)–(14). Fig. 3(b) shows the L distribution with the stray light removed, showing that the distribution is now continuous and smooth. Furthermore, unexpected from the standpoint of the original algorithm is the change in radiance drop-off behavior for $\theta_s \sim 97°$ and larger. The radiance behavior in this regime results from airglow contributions, which will be discussed in the following section.

C. Airglow Impacts on the GVVSSE/GVVSLE LUTs

As previously discussed, the DNB radiance should fall exponentially, for $\theta_s > 97°$. However, due to the presence of airglow [6] in the DNB observations, the radiances instead fall off as a function of θ_s according to Fig. 3(c) (solar curve). The airglow comprises a variety of chemiluminescent reactions, predominantly those involving excited-state hydroxyls, atomic and molecular oxygen, and atomic sodium. These account for emissions in the visible to near-infrared, with peak emissions near the mesopause (~87 km). The airglow can be subdivided into three categories: dayglow, twilight glow, and nightglow. The category relevant to the DNB measurements, and the NCC

processing, particularly on moonless nights, is the nightglow, which corresponds only to the illumination the DNB observes beyond twilight. Note: some fraction of the nightglow may be due to starlight and zodiacal light as well. The VIIRS DNB is sensitive enough to sense both the direct emission of nightglow as well as the reflection of the nightglow signal off clouds and the surface during moonless nights, with radiance values on the order of $\sim 10^{-10}$ W/cm^2/sr [10].

If nightglow were not detectable by the DNB, the radiances for $\theta_s > 97^\circ$ would fall off exponentially as it does for θ_s between 90° and 97° down to the noise floor of the sensor. However, because the nightglow essentially acts as an extra source of illumination (both via direct emission and reflectance off clouds and the surface), the radiances from $\theta_s = 97^\circ$ to 105° fall off at a much slower rate than what would have been otherwise extrapolated from θ_s between 90° and 97° [see Fig. 3(c)]. The final solar $L_{\rm fit}$ curve is shown as the solid line in Fig. 3(c). In this processing scheme, the nightglow is only accounted for by the solar curve; the lunar curve [dashed line in Fig. 3(c)] is assumed to fall at the same rate for $\theta_l \geq 90^\circ$ in order to avoid the double counting of the nightglow contribution in the gain calculations. The final gain values derived from the normalized radiances in Fig. 3(c) are shown in Fig. 3(d).

Because the new GVVSSE table must account for nightglow, the methodology to construct the GVVSSE/GVVSLE LUT described in Section III-A is modified. For θ_s between 0° and 97°, G_l and G_s are identical. The nightglow region is partitioned into two regions for $\theta_s \geq 97^\circ$, which take on the following function forms:

$$L^4_{\rm fit}(\theta_s) = e^{d_0 + d_1\theta_s + d_2 + \theta_s^2 + b_3\theta_s^3 + b_4\theta_s^4} \quad (15)$$

$$L^5_{\rm fit}(\theta_s) = e^{e_0 + e_1\theta_s} \quad (16)$$

where (15) and (16) are valid for $\theta_3 \leq \theta_s \leq \theta_4$ and $\theta_4 \leq \theta_s \leq 180$, respectively (fits are done on the natural log of the empirical functions). These functions have the same boundary conditions as (12) and (13), where $i = 1{-}4$ for (9)–(11), (15), and (16). The angles that produce the best fit for the August 16–18, 2012, data [in Fig. 3(c)] are the following: $\theta_1 = 86^\circ$, $\theta_2 = 91^\circ$, $\theta_3 = 97^\circ$, and $\theta_4 = 105^\circ$.

For $\theta_s = 97^\circ{-}105^\circ$ (15), the fitted function needs to bend away from the rapid exponential fall-off. Airglow is actually present for $\theta_s \geq 90^\circ$ (i.e., twilight glow and dayglow), but since the twilight radiances due to Rayleigh (molecular) scattering are much brighter than the twilight glow, the twilight glow cannot be discerned until $\theta_s \sim 97^\circ$. After 105° (16), the nightglow falls off at a much slower rate than the fall-off between 90° and 97°. This corroborates previous findings that the nightglow is largely independent of solar zenith angle [12].

The lunar gain G_l preserves the same exponential increase (or fall-off in radiance units) from ~97° out to ~105°. From 105°, the gains are kept constant to keep the values from becoming too large; computationally, the gains can, otherwise, reach an overflow condition, leading to values of infinity if allowed to exponentially increase (or fall-off in radiance units) for lunar angles out to 180° [see Fig. 3(d)]. Since the lunar irradiance value scales inversely to G_l, the reference radiance $L_{{\rm ref},l}$ [(4)] will become negligible compared to $L_{{\rm ref},s}$ for these larger θ_l.

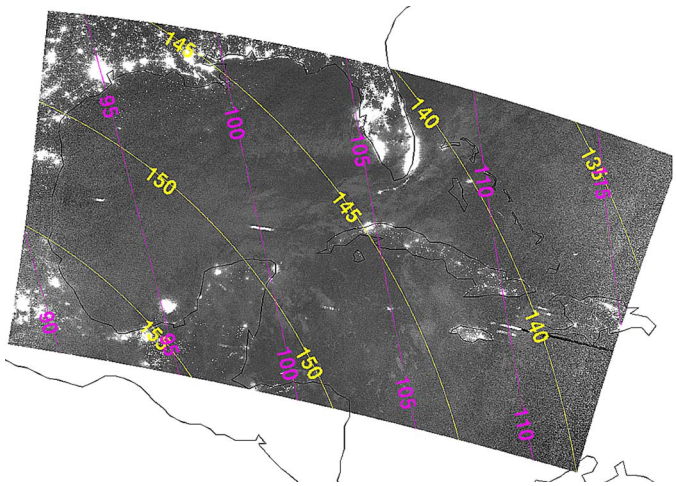

Fig. 4. VIIRS NCC maps taken on September 24, 2012, between 07:10 and 07:15 UTC (near first quarter moon condition) that result from algorithm thresholds and LUT modifications described previously. Original operational map shows fill values for all pixels. Yellow and magenta contours are θ_s and θ_l, respectively, in increments of 5°. Map is on a Mercator projection.

IV. Results

The gains (G_s and G_l) computed via (14) and derived from (9)–(11) and (15) and (16) are used by (3) and (4) to compute the NCC pseudo-albedo α in (2). With the algorithm threshold and the GVVSSE/GVVSLE adjustments, the NCC EDR algorithm produces imagery for all solar and lunar conditions. Fig. 4 shows a composite of three continuous NCC nighttime granules taken near a first quarter moon on September 24, 2012, from 07:10 to 07:15 UTC; yellow and pink curves are θ_s and θ_l contours. This particular case was selected because it provides an example of improved NCC algorithm behavior in the vicinity of the lunar terminator. The original operational NCC product showed no imagery (not shown) because the algorithm does not produce imagery for θ_s and $\theta_l > 105^\circ$ (i.e., a case when no appreciable sunlight or moonlight should be present in the scene). In addition, there was no imagery for $\theta_s > 105^\circ$ and $\theta_l \leq 105^\circ$ because $\alpha \gg 5$ in this scenario, where $L_{{\rm ref},s} = 0$ and $L_{{\rm ref},l}$ is very small. The resultant NCC imagery after the algorithm thresholds and gain adjustments are applied reveals city lights, lightning strikes (e.g., horizontal white streak crossing the $\theta_l = 100^\circ$ contour line), and faint cloud features. One of the most useful features of NCC imagery, and its originally intended purpose, is to identify atmospheric features in the vicinity of the solar terminator. However, since the NCC imagery now will extend to $\theta_s > 105^\circ$, it will be possible to observe atmospheric features throughout the day and night, including astronomical dark conditions beyond the lunar terminator as well.

Fig. 5 shows 22 contiguous NCC granules collected on October 19, 2012, between 12:20 and 12:50 UTC (near new moon conditions). City lights, detailed cloud structures, and storm systems can be observed simultaneously; the transition between day and night is almost indiscernible. Toward the southern portion of the map in Fig. 5, the image looks more grainy or noisy because the radiances of the night granules are near the VIIRS $L_{\rm min}$ value of 3×10^{-9} W/cm^2/sr. Even so,

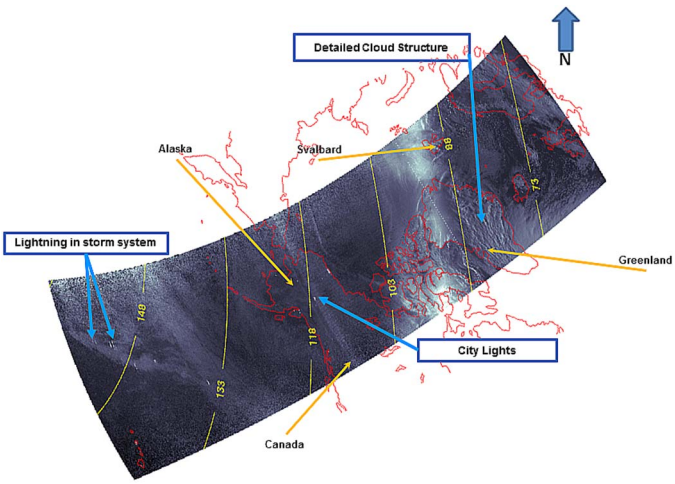

Fig. 5. Twenty-two continuous NCC granules, with new LUT threshold and gain adjustments, taken from October 19, 2012, from 12:20 to 12:50 UTC. The granules span day and night as indicated by the solar zenith angle contours (yellow). Features such as detailed clouds, city lights, and a storm system are highlighted. Map is on an equidistant azimuthal projection.

the VIIRS DNB has SNR > 9 at $L_{\min}$, which provides more than enough signal to identify atmospheric features although with reduced quality as compared to pixels around nadir; SNR at nadir is about 3–4 times better than at the edge-of-scan [3]. One thing to note is the bright horizontal structure between θ_s of 88° and 103°. This artifact is a result of a combination of atmospheric (Rayleigh) scattering and cloud scattering in the twilight region; Section V will provide further details.

V. Outstanding Issues

The LUTs derived using the methodology described in Section III-A and the updates described in Section III-C have recently been implemented in the Interface Data Processing Segment (IDPS) operational system and have been in operations since July 10, 2013; IDPS is now producing imagery for all solar and lunar conditions. Although the new LUTs account for the solar, lunar, and observed nightglow, two other illumination sources have not been accounted for: scattering by atmospheric constituents and clouds. The current algorithm only takes into account TOA radiances resulting from solar, lunar, and nightglow reflection and scattering (nightglow emission as well) off the surface and the tops of clouds. However, during twilight ($\theta_s \sim 90°-98°$), atmospheric scattering becomes the dominant source of illumination, and its relationship to solar zenith angle is not straightforward. High-level clouds are also fully illuminated by the sun for θ_s out to $\sim 94°$. Together, these cause a large contrast that cannot be easily corrected by a single gain as a function of θ_s. Fig. 6 highlights the scattering by the atmosphere and clouds. Note: the bright band that runs through western and eastern Europe (through the $\theta_s = 120$ contour line) is residual stray light. Right before reaching northern Europe, a bright band spans, in the scan direction, solar angles between $\theta_s \sim 90°$ and 100°. The bright envelope is a result of Rayleigh scattering in the atmosphere and becomes more pronounced toward the edge of the scan. Furthermore, the

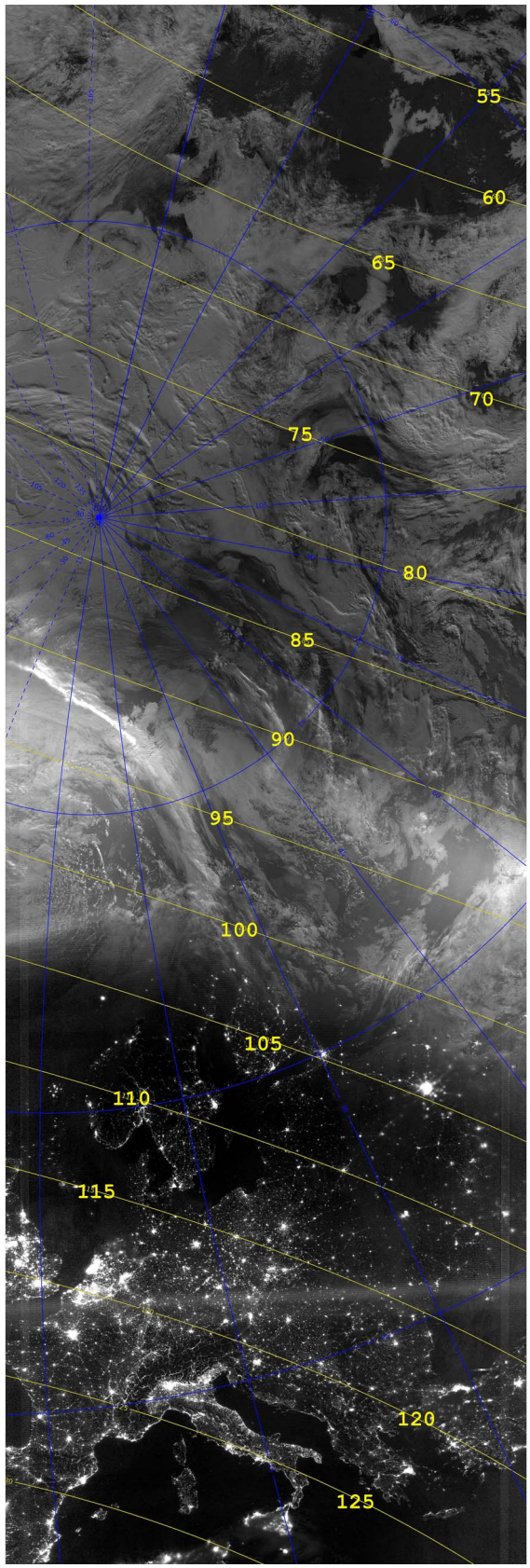

Fig. 6. VIIRS NCC pseudo-albedo gray-scale image for September 4, 2012, from UTC 00:35 to 00:58. Yellow contours are for solar zenith angles where the higher solar angles start from the top right of the image and increase toward night at the bottom left of the image. The bright dim band across western and eastern Europe (runs through the "120" θ_s contour line) is uncorrected residual DNB stray light.

cloud scattering near the edge-of-scan is acting as sources of illumination. Because both the atmospheric and cloud effects are not accounted for in the NCC algorithm, IDPS will continue to produce NCC that really should be considered a gray-scale image rather than a pseudo-albedo. To remove these effects would require modeling the scattering impacts in the terminator for a variety of atmospheric and cloudy conditions, which is challenging to do given that many radiative transfer models do not account for the spherical geometry of the Earth very well [11]. However, rather than use radiative transfer modeling, some improvement could possibly be achieved by producing f_s and f_l from empirical data, as is currently done for G_s and G_l. This would require binning the empirical data into a 3-D grid, compared with one dimension for the current process used for G_s and G_l. Nevertheless, even with these issues, the NCC product highlights the unprecedented capability of the VIIRS DNB to characterize the evolution of atmospheric, surface, and cloud features during twilight and nighttime and serves as a valuable aid for the weather forecasting community.

VI. Conclusion

We have investigated the root causes for the suboptimal at-launch NCC product performance and have developed a solution to address the stray light contamination and nightglow-related issues. Fitting functions were derived in four angular regimes using a χ^2 minimization algorithm to produce the best fits of gain versus θ_s and θ_l. The boundary conditions in (12) and (13) serve to produce continuous functions to reduce any visual discontinuities. This solution, implemented in IDPS on July 10, 2013, has provided NCC imagery under all illumination conditions. We do note that the high contrast due to atmospheric and cloud scattering in the twilight region does produce artifacts that, currently, are not removed given the challenging nature of modeling these effects. However, the weather forecasting community has already benefited from having continuous production of NCC imagery. Visible imagery for clouds in low-light conditions provides complementary information to thermal infrared imagery of weather phenomena such as hurricanes or storm systems, thus assisting forecasters with tracking storms, the presence of fog and low clouds, snow cover, biomass smoke, lofted dust, and a host of other general environmental characterization capabilities [13]. Furthermore, because the solar and lunar variation has been removed in the NCC imagery, it is possible to observe the diurnal variation of these weather phenomena.

Acknowledgment

The work presented herein, in part, was performed under Northrop Grumman AMS Contract 1707, NPP Mission Support. C. K. Liang would like to thank T. Ohnuki for the many helpful discussions on the NCC algorithm and M. Kowitt for clarifying many aspects of how the model inputs were generated. S. Mills would like to thank T. Ohnuki and D. Searcy, who did much of the original programming and testing of the NCC algorithm at Northrop Grumman.

References

[1] C. D. Elvidge, K. E. Baugh, A. Kihn, H. W. Kroehl, and E. R. Davis, "Mapping city lights with nighttime data from the DMSP Operational Linescan System," *Photogramm. Eng. Remote Sens.*, vol. 63, no. 6, pp. 727–734, Jun. 1997.

[2] H. Letu, M. Hara, G. Tana, and F. Nishio, "A saturated light correction method for DMSP/OLS nighttime satellite imagery," *IEEE Trans. Geosci. Remote Sens.*, vol. 50, no. 2, pp. 389–396, Feb. 2012.

[3] L. B. Liao, S. Weiss, S. Mills, and B. Hauss, Suomi NPP VIIRS day–night band on-orbit performance, *J. Geophys. Res. Atmos.*, vol. 118, no. 22, pp. 12 705–12 718, Nov. 2013.

[4] R. W. Lieske, "Technical Operating Report for Block 5D-3 Operational Linescan System (OLS)," Westinghouse Defense and Electronic Systems Center, Baltimore, MD, USA, 1993.

[5] "VIIRS Imagery Products Algorithm Theoretical Basis Document (ATBD)," Goddard Space Flight Center, Greenbelt, MD, USA, p. 666.

[6] M. F. Ingham, "The light of the night sky and the interplanetary medium," *Rep. Progr. Phys.*, vol. 34, no. 3, pp. 875–912, Sep. 1971.

[7] S. P. Mills, S. C. Weiss, and C. K. Liang, "VIIRS day/night band (DNB) stray light characterization and correction," in *SPIE Opt. Eng. Appl.*, 2013, vol. 8866, pp. 88661P-1–88661P-18.

[8] Goddard Space Flight Center, JPSS VIIRS Control Data Format Control Book External (CDFCB-X) Volume VIII-Look Up Table Formats, pp. 32–43, Greenbelt, MD, USA 2011.

[9] Raytheon ITSS, VIIRS Imagery Unit Level Detailed Design Document, p. 37, Lanham, MD, USA 2002.

[10] S. D. Miller, S. P. Mills, C. D. Elvidge, D. T. Lindsey, T. F. Lee, and J. D. Hawkins, "Suomi satellite brings to light a unique frontier of nighttime environmental sensing capabilities," *Proc. Nat. Acad. Sci.*, vol. 109, no. 39, pp. 15 706–15 711, Sep. 2012.

[11] S. P. Mills, S. C. Weiss, T. Ohnuki, D. Searcy, M. Plonski, E. Jacobson, J. McCarthy, and J. Jaron, "Calibration of the VIIRS day/night band (DNB)," in *Proc. AMS 6th Annu. Symp. Future Natl. Oper. Env. Satellite Syst.-NPOESS-GOES-R*, 2010, pp. 1–9.

[12] J. Xu, A. K. Smith, G. Jiang, H. Gao, Y. Wei, M. G. Mlynczak, and J. M. Russell, III, "Strong longitudinal variations in the OH nightglow," *Geophys. Res. Lett.*, vol. 37, no. 21, pp. L21801-1–L21801-6, Nov. 2010.

[13] S. D. Miller, W. Straka, III, S. P. Mills, C. D. Elvidge, T. F. Lee, J. Solbrig, A. Walther, A. K. Heidinger, and S. C. Weiss, "In sunshine and in shadow: Illuminating the capabilities of the Suomi NPP VIIRS day/night band," *Remote Sens.*, vol. 5, pp. 6717–6766, Dec. 2013.

[14] Q. L. Zhang, C. Schaaf, and K. C. Seto, "The vegetation adjusted NTL urban index: A new approach to reduce saturation and increase variation in nighttime luminosity," *Remote Sens. Environ.*, vol. 129, pp. 32–41, Feb. 2013.

[15] D. Ziskin, K. Baugh, C. H. Feng, F. Ghosh, and C. D. Elvidge, "Methods used for the 2006 radiances lights," in *Proc. 30th Asia-Pac. Adv. Netw. Meet.*, 2010, pp. 131–142.

Calvin K. Liang received the physics A.B. from Occidental College, Los Angeles, CA, USA, and the M.S. and Ph.D. degrees in atmospheric and oceanic sciences from the University of California, Los Angeles, CA, USA.

He has worked on the Suomi-NPP program for the last 12 years at Northrop Grumman Corporation, Redondo Beach, CA, USA. He is an expert in remote sensing and its usage in climate science applications. He has been the lead or coauthor of many publications on the subject of using remote sensing instruments for climate studies. Most notable is his work showing that El Niño Southern Oscillation (ENSO) and Quasi-biennial Oscillation (QBO) have a dual impact on the concentration of water vapor that enters the tropical stratosphere. His most recent work also showed how ENSO and QBO, in concert with the Brewer–Dobson circulation, impact the tropical tropopause layer cloud distribution. He has been a reviewer for GRL, ACP, and other leading geophysical journals.

Stephen Mills received the B.S. degree in physics from the University of California, Los Angeles, CA, USA, and the M.S. degree in physics from California State University, Los Angeles.

He is the founder of Renaissance Man Engineering. He has 13 years of experience in satellite remote sensing and 35 years in aerospace instrumentation. At Northrop Grumman Corporation, Redondo Beach, CA, USA, he headed the VIIRS Radiometric Calibration Group for the Suomi-NPP program before taking early retirement. He is a world-class expert in remote sensing and has numerous publications on the subject. He is also a member of the Engineering Advisory Council at Stellar Solutions Inc., Palo Alto, CA, USA.

Bruce I. Hauss received the B.S. degree in physics and the M.S. and Ph.D. degrees in nuclear engineering from the University of California, Los Angeles, CA, USA.

He was a Northrop Grumman Corporation (NGC) Technical Fellow and the Head of the Sensor Signatures and Analysis Section, Sensors, Lasers and Research Center. He has over 30 years of modeling and simulation experience, with technical expertise in the phenomenology, analysis, and simulation of sensor signatures from RF to UV, radiative transfer, environmental remote sensing, and computer modeling and simulation. He served as the principal architect of EVEREST, NGCs integrated weather product testbed, managing the efforts of both internal resources and subcontractors to develop new modeling and simulation capabilities. He also served as the Test Data Generation Lead in the NPOESS (now Suomi-NPP) Systems Engineering IPT, heading the development of new simulation capabilities for emulating measurements from the NPOESS sensors/spacecraft system and developing global test data sets for prelaunch verification of the spacecraft, sensors, and their environmental data product retrieval algorithms. He currently continues to support NGC's remote sensing and weather modeling/simulation efforts as a consultant through DKK Company Inc., Ruston, LA, USA.

Steven D. Miller received the B.S. degree in electrical and computer engineering from the University of California, San Diego, La Jolla, CA, USA, and the M.S. and Ph.D. degrees in atmospheric science from Colorado State University (CSU), Fort Collins, CO, USA.

While at the Naval Research Laboratory in Monterey, he conducted research in satellite meteorological application development based on a wide array of passive/active satellite sensors and model-fusion techniques for detection and characterization of clouds/fog, precipitation, dust, volcanic ash, snow cover, and fires. He now serves as the Deputy Director and Senior Research Scientist of the Cooperative Institute for Research in the Atmosphere, CSU. His current research centers on the use of low-light visible sensors to improve characterization of the nocturnal environment. Notable publications in this regard include the first satellite detection of Milky Sea bioluminescence using data from the Defense Meteorological Satellite Program Operational Linescan System, a lunar model enabling nighttime cloud optical depth retrievals from moonlight reflectance, and the unprecedented ability of the Suomi National Polar-orbiting Partnership day/night band sensor to utilize airglow illumination for meteorological imagery.